

12. Takeishi Y, Sukekawa H, Saito H, et al. Clinical significance of decreased myocardial uptake of ^{123}I -BMIPP in patients with stable effort angina pectoris. *Nucl Med Commun* 1995;16:1002-1008.
13. Takeishi Y, Sukekawa H, Fujiwara S, Ikeno E, Sasaki Y, Tomoike H. Reverse redistribution of $^{99\text{m}}\text{Tc}$ -sestamibi following direct PTCA in acute myocardial infarction. *J Nucl Med* 1996;37:1289-1294.
14. Fujiwara S, Takeishi Y, Atsumi H, Takahashi K, Tomoike H. Fatty acid metabolic imaging for the diagnosis of coronary artery disease. *J Nucl Med* 1997; 37:175-180.
15. Yamamichi Y, Kusuoka H, Morishita K, et al. Metabolism of iodine-123-BMIPP in perfused rat hearts. *J Nucl Med* 1995;36:1043-1050.
16. Tamaki N, Kawamoto M, Yonekura Y, et al. Decreased uptake of I-123 BMIPP as a sign of enhanced glucose utilization assessed by FDG-PET [Abstract]. *J Nucl Med* 1991;32:1034.
17. Gregoire J, Theroux P. Detection and assessment of unstable angina using myocardial perfusion imaging: comparison between technetium-99m sestamibi SPECT and 12-lead electrocardiogram. *Am J Cardiol* 1990;66:42E-46E.
18. Bilodeau L, Theroux P, Gregoire J, Gagnon D, Arsenaault A. Technetium-99m sestamibi tomography in patients with spontaneous chest pain: correlations with clinical, electrocardiographic and angiographic findings. *J Am Coll Cardiol* 1991;18:1684-1691.

Image Enhancement of Severely Hypoperfused Myocardia for Computation of Tomographic Ejection Fraction

Kenneth Nichols, E. Gordon DePuey, Alan Rozanski, Helene Salensky and Marvin I. Friedman

Department of Radiology and Division of Cardiology, St. Luke's-Roosevelt Hospital and Columbia University College of Physicians and Surgeons, New York, New York

Ejection fractions computed from $^{99\text{m}}\text{Tc}$ -sestamibi myocardial perfusion gated tomograms have demonstrated a high degree of accuracy and reproducibility. Although automated algorithms appear to provide reasonable endocardial outlines for patients over a broad spectrum of cardiac diseases, in cases of severe hypoperfusion, it is necessary to manually adjust contrast and brightness to judge whether borders are correct or must be altered. **Methods:** Midventricular horizontal and vertical long axis gated tomograms were generated for 116 studies chosen on the basis of extensive, severe myocardial perfusion defects. Automated software transformed cinematic tomograms into images demonstrating uniform appearance of the myocardium throughout the cardiac cycle. Transformed images were introduced to edge detection algorithms for subsequent calculation of ventricular volumes and ejection fractions. **Results:** Linear regression analysis demonstrated excellent intraobserver reproducibility for ejection fractions ($r = 0.95$) and volumes ($r = 0.98$). There was also good agreement of ejection fractions ($r = 0.86$) and volumes ($r = 0.94$) with values derived from an expert's manual drawings. In a subgroup of 22 patients, automated ejection fractions from transformed images demonstrated better agreement with independent first-pass values ($r = 0.90$) than did manual measurements derived from original data ($r = 0.85$). **Conclusion:** Image enhancement algorithms succeeded in providing accurate, reproducible gated SPECT ejection fractions in the most difficult class of patients exhibiting severe hypoperfusion.

Key Words: gated SPECT; image enhancement; ejection fraction
J Nucl Med 1997; 38:1411-1417

The importance of left ventricular (LV) ejection fraction (EF) measurements in the clinical management of cardiac patients is well established (1,2). EF calculations using $^{99\text{m}}\text{Tc}$ -sestamibi myocardial perfusion gated tomograms have been reported using different approaches, including simple manual techniques (3,4), relaxation labeling combined with computed wall thickening (5,6) and Gaussian midmyocardial detection (7). Excellent reproducibility of gated SPECT EF has been reported (8), and these measurements correlate well with those obtained by gated blood pool equilibrium studies (9,10), first-pass radionuclide angiography (7,9,11,12), echocardiography (13), magnetic resonance imaging (5,14) and x-ray contrast ventriculography

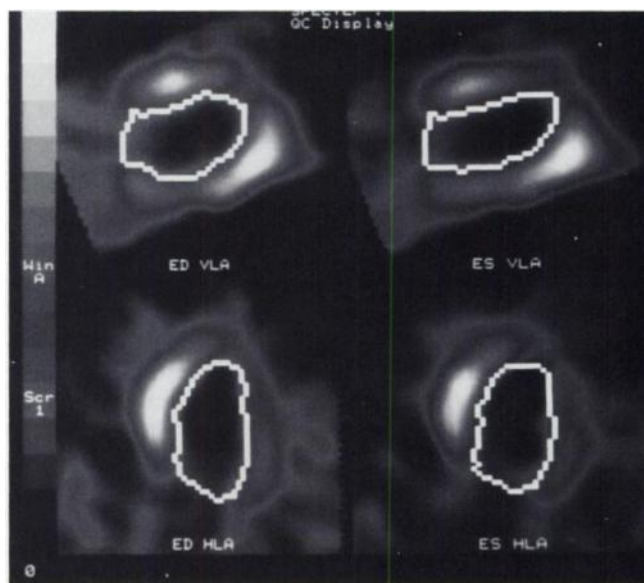


FIGURE 1. Automatic endocardial borders for a case of severe hypoperfusion of the apico-lateral territories.

(4,11). Additionally, gated SPECT EF processing has been automated successfully (7,9), as has selection of LV limits and axes needed to provide input to gated SPECT EF software (15,16).

Despite these validations and regardless of which computational method is used, proper interpretation of myocardial perfusion tomograms remains problematic in cases of severe myocardial hypoperfusion (Fig. 1). Endocardial borders shown in Figure 1 were generated automatically (9), and although these are plausible, it is difficult to ascertain whether these truly represent the actual myocardium because the apico-lateral wall is nearly invisible in horizontal long axis (HLA) images and because apical counts are greatly reduced in vertical long axis (VLA) views. In addition, greatly reduced counts can defeat algorithms, which are based on gated SPECT count densities, designed to detect heart walls.

It is important to review images in recognizing and compensating for artifacts in interpreting studies (17,18). Yet, some gated SPECT EF methods are largely divorced from a visual appreciation of original myocardial perfusion images, despite displaying final results in four dimensions (5,7). Some auto-

Received Sep. 12, 1996; revision accepted Feb. 3, 1997.

For correspondence or reprints contact: Kenneth Nichols, PhD, Division of Cardiology, St. Luke's-Roosevelt Hospital, Amsterdam Avenue at 114th St., New York, NY 10025.

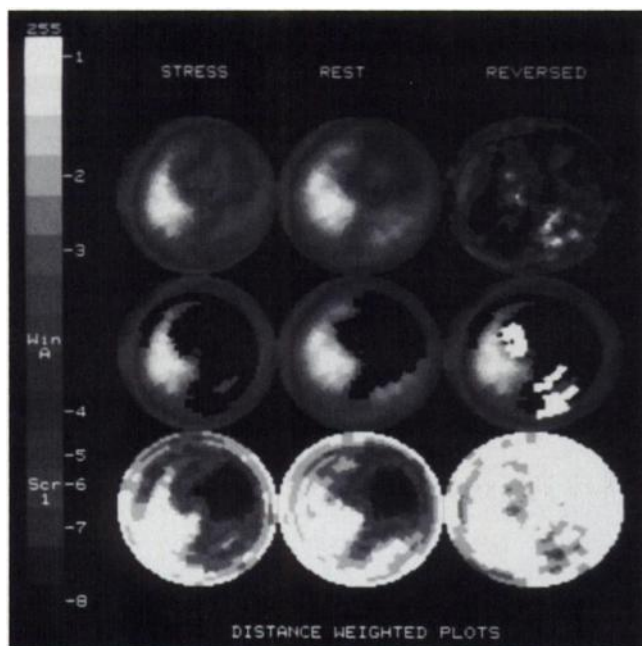


FIGURE 2. Stress and rest perfusion polar maps corresponding to the myocardial perfusion images of Figure 1.

mated techniques show few intermediate steps during execution (7,16), whereas others rely on Fourier fits to time series of perfusion polar maps, which observers do not see as part of data review (5,6). Only one gated SPECT EF method altered the display of original gated tomograms through image inversion (11,19) but more as a preprocessing step to enhance edges than as an aid in visual interpretation.

Visual verification of success of endocardial border identification is always important, and in cases of severe hypoperfusion, observers must adjust contrast and brightness of computer displays and must do so manually, to decide whether they are satisfied with results and to aid in effecting edge changes. Therefore, we sought to simultaneously address issues of improving algorithmic endocardial border detection and of visual verification by automatically altering regional contrast of gated myocardial perfusion tomograms, our main goal being to augment quality assurance of automated EF calculations in cases of severe hypoperfusion. The approach that was chosen was to produce transformed images that optimally depict myocardial walls throughout the cardiac cycle. In the process, two types of "mapped" cinematic images were generated of use to observers: "brightening-mapping," for aiding visual appreciation of myocardial wall thickening, and "motion-mapping," to facilitate discernment of regional wall translation associated with ventricular contraction.

MATERIALS AND METHODS

Patients

Technetium-99m stress myocardial perfusion data from January 1, 1992, to December 31, 1995, were reviewed retrospectively, and from this data, 123 patient studies were selected at random solely on the basis of exhibiting severe myocardial hypoperfusion, defined by stress quantitative perfusion polar maps with defect counts below 15% of normal maximum counts, along with defect extent >25% of polar map area (Fig. 2). Seven of these studies were subsequently discarded when it was found that splanchnic activity greatly exceeded severely hypoperfused LV inferior wall myocardial activity. No other criteria were imposed to select or exclude patient data. The 116 remaining patients (aged 66 ± 13 yr; 58% men) were characterized by quantitative perfusion polar map

"defect extent" of 167 ± 58 and "defect severity" of 830 ± 394 (20). Defect count density was $7\% \pm 3\%$ of normal maximum myocardial counts.

First-Pass Imaging

Among patients studied were a subgroup of 22 (aged 60 ± 10 yr; 50% men) who also had gated first-pass (GFP) Anger camera data acquisitions of the 814 MBq of ^{99m}Tc -sestamibi bolus used for the resting portion of a 2-day sestamibi perfusion protocol (21). Their perfusion scans exhibited quantitative perfusion polar map defect extent of 152 ± 64 and defect severity of 719 ± 365 (20). Defect count density was $7\% \pm 3\%$ of normal maximum myocardial counts. Quality assurance criteria were applied such that GFP studies were discarded if bolus transit time exceeded 2.0 sec or if lung transit time exceeded 10 heart beats. All GFP data were analyzed by software previously validated against both equilibrium gated blood pool and multicrystal first-pass gamma camera correlative studies (22).

Gated SPECT Imaging

Technetium-99m-sestamibi injections were performed during peak exercise of a Bruce protocol with a treadmill using 1.11 GBq for a 1-day protocol or 814 MBq for a separate-day protocol (21). Tomograms (64×64) with a pixel size of 6.4 mm were acquired with high-resolution collimation for 20 sec at 64 projections over 180° with a biplane camera so that acquisitions were performed in 12 min. Tomograms were acquired of the stress perfusion distribution with patients at rest, greater than 30 min after stress, at 8 frames per R-R interval with a 100% beat acceptance window.

Standard clinical data processing parameters were used (20): Butterworth (0.40,10) prefilters for gated tomograms, followed by quantitative ramp x-filtering (23), interslice spatial averaging and time-filtering among the eight gated frames. Images were reoriented into VLA, HLA and short axis (SA) sections using manual choices by an observer of anterior, inferior, septal and lateral limits and approximate LV symmetry axes. Commercially available software (20) was used to produce stress and rest perfusion polar maps (Fig. 2) from SA images and to generate cinematic midventricular VLA and HLA images. These cinematic tomograms were input to previously described software that automatically generated endocardial borders on end-diastolic (ED) and end-systolic (ES) frames (9). An observer had the option of altering automated LV centers, ED and ES frame identification and endocardial borders. During automatic endocardial border generation (Fig. 1), estimated points of intersection of the valve plane with the myocardium from ED and ES images were output to a computer file for later use by image transformation algorithms described below. Subsequent transformations were performed from the valve plane forward to the apex, but for the valve plane to the outflow tract, transformations were modulated linearly to leave outflow tract counts unaltered and dark.

Image Transformations

In the simple regional contrast transformation, referred to here as brightening-mapping, a radial search was performed in 2° increments at every angle, θ , of the centered ED VLA frame to find the local maximum count, $D^{\max}(\theta)$ (Fig. 3). Then the factor, $f(\theta)$, needed to boost $D^{\max}(\theta)$ up to the maximum myocardial count of the entire image, M^{\max} , was computed as $f(\theta) = M^{\max}/D^{\max}(\theta)$. Finally, the counts, $c[r,\theta]$, in each radial pixel at fixed angle θ were multiplied by that factor $f(\theta)$ along the entire radius, r , of the input image to form the output transformed ED image. This mapping rendered the ED midmyocardium uniformly bright. The same set of ED angular factors, $f(\theta)$, were then applied to all other frames to reveal relative percentage of regional brightening (Fig. 3). This was postulated to reflect myocardial thickening by way of well-known

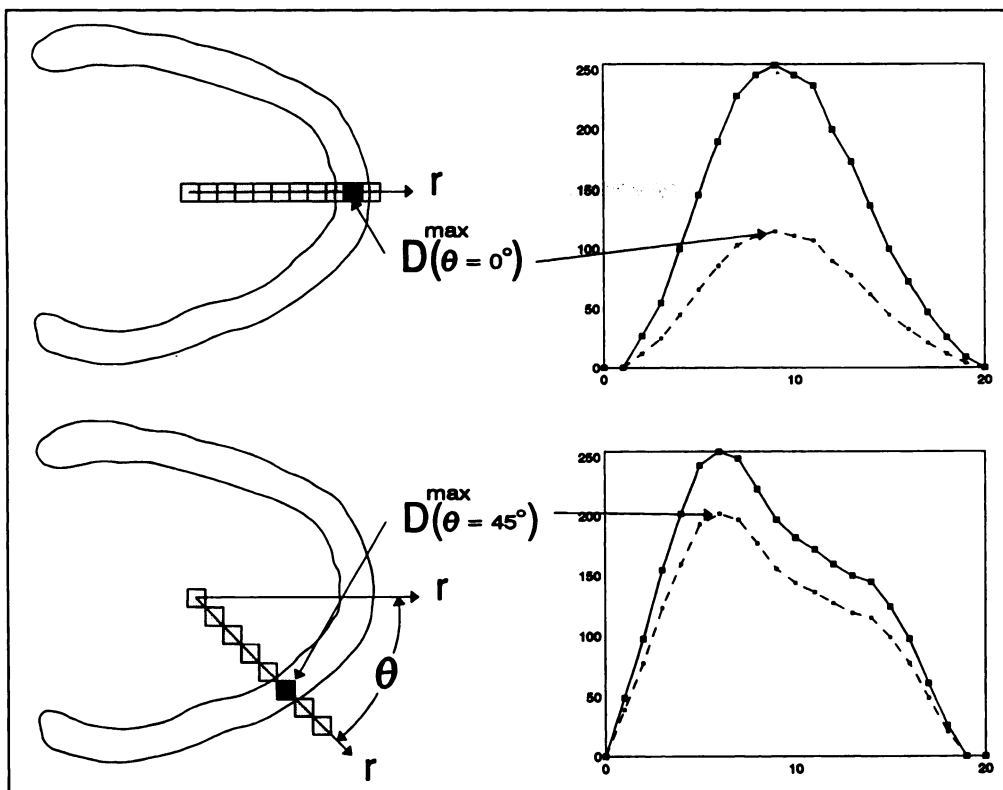


FIGURE 3. A schematic of the image transformations. The top left depicts the set of radial pixels through the apical VLA image at angle $\theta = 0^\circ$, with a maximum count $D^{\max}(\theta=0^\circ)$ of 115 counts at the middle of the myocardium. The radial count profile along that ray is shown (dashed line) in the graph at the top right. This input curve was multiplied by the factor necessary to bring the maximum of the output curve (solid line) up to 255 counts. The bottom left depicts the set of radial pixels through the infero-apical $\theta = 45^\circ$ angle, with a maximum myocardial count $D^{\max}(\theta=45^\circ)$ of 202 counts. The radial count profile along the ray at $\theta = 45^\circ$ is shown (dashed line) in the graph at the bottom right, which was multiplied by a different factor needed to produce an output curve (solid line) at the same new 255 count maximum level. This process was performed at every angle in 2° increments. The input curves shown here are taken from the VLA images of Figure 1.

partial volume effects (24). Other investigators have computed polar myocardial thickening maps analogous to perfusion polar maps (6,19,25), but the implications of this approach had not previously been rendered visualizable. The midmyocardial ED HLA tomogram was then used to find a new set of factors, $f(\theta)$, which were applied to all midmyocardial HLA cinematic frames.

The motion-mapping algorithm differed from that of brightening-mapping only in that angular mapping factors $f(\theta)$ were determined from and applied to each cinematic frame separately. Because the maximum radial count at every angle of every frame was used as the basis of normalizing each ray of each cinematic image, this transformation provided uniform appearance of the myocardium for every frame throughout the cardiac cycle, at the expense of any impression of brightening.

Effects of brightening-mapping and motion-mapping are illustrated in Figure 4 for the same patient data input. In the example

shown, only the infero-apical territory brightened and only by a small amount. The corresponding ED brightening-mapped image demonstrated a uniform appearance of the myocardium, as expected, but at ES areas of lowest count density intensified in discrete, disconnected "globules." Anomalous count density "gaps" have also been observed in some brightening-mapping-transformed images. These globules and gaps were merely noise artifacts, which would be distracting if the goal were to identify either midmyocardial or endocardial points. However, there were no noise artifacts for motion-mapped images at ES and, as expected, no systolic brightening (Fig. 4). Thus, for purposes of tracking endocardium, either visually or algorithmically, motion-mapping provided more consistent and more easily interpretable input images than either original data or brightening-mapped images. For this reason, motion-mapped images and not brighten-

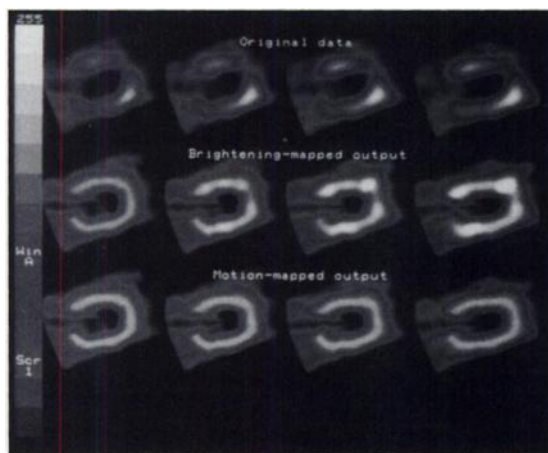


FIGURE 4. The results of the radial image transformations. The top row shows the original four cinematic midventricular VLA tomograms from ED on the left to ES on the right. The middle row consists of brightening-mapped output images, and the bottom row displays corresponding motion-mapped images. The example shown is for the same patient of Figures 1-3.

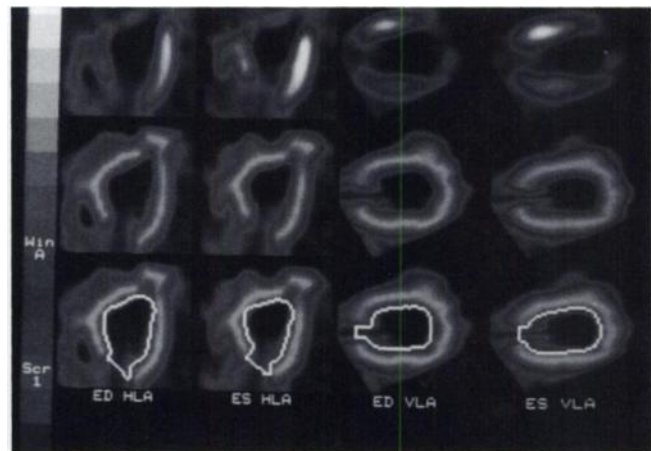


FIGURE 5. The use of HLA and VLA motion-mapped images for endocardial border generation is illustrated for a patient exhibiting severe hypoperfusion of the infero-apical territories. The top row shows the original images at ED and ES, the middle row shows the motion-mapped images and the bottom row shows the automatically determined endocardial borders, as generated using the motion-mapped images as input.

TABLE 1
Intraobserver Reproducibility of Motion-Mapped Parameters:
Linear Regression Analysis

Parameter	N	r	Intercept	Slope	SEE
EF	116	0.95	0.9%	0.97	4.5%
EDV	116	0.98	5.0 ml	0.96	13.2 ml
ESV	116	0.98	2.9 ml	0.97	13.0 ml
ΔEF	116	0.07	-1.1%	0.02	4.5%
ΔEDV	116	0.01	2.3 ml	-0.02	13.4 ml
ΔESV	116	0.03	0.8 ml	-0.01	13.1 ml

ing-mapped images were used for automated endocardial edge detection as shown in Figure 5.

It was not necessary to alter existing edge-tracking software (9) to generate automatically the endocardial borders of Figure 5. Rather, it was sufficient to normalize input images to the appropriate maximum count level because previously written algorithms assumed input data would always have the same normalized maximum counts. The final VLA and HLA endocardial border dimensions were then corrected for the camera's line spread function and combined to compute ventricular volumes and EF values with the Simpson's rule formula (3).

Manual Computations

In the absence of algorithms to enhance visual appearance of the myocardium, EF values computed from severely hypoperfused myocardial perfusion gated SPECT studies would have required careful review by an observer who was experienced in analysis of such data. Therefore, an observer who was already well versed in manual methods (3) reviewed VLA and HLA ED and ES images along with the cinematic playback of these data using simultaneous monochrome and color displays, while manually drawing endocardial borders. The observer was free to alter contrast and brightness of all displays to derive as much helpful information as possible as to likely locations of the endocardium. These edges were then used for independent computation of LV volumes and EF values, as previously described (3,9).

Statistical Analysis

All numerical results are reported as mean values \pm s.d. Linear regression analysis was used to compare calculations of LV volumes and EF values among independent observations and between modalities. Linear regression analysis was also performed in conjunction with Bland-Altman analysis of differences versus averages of paired values, to search for trends and systematic errors (26,27). Paired Student's t-tests were used to compute two-tailed probabilities (p) that measurements were substantially different in comparing two techniques, with p values < 0.05 considered to be statistically significant. Statistical significance of two different regression results was assessed with the Fisher Z-test.

RESULTS

Reproducibility

EF processing was highly reproducible (Table 1). There was excellent agreement between EF values computed indepen-

TABLE 2
Intraobserver Reproducibility of Motion-Mapped Parameters:
Paired t-Test Results

Parameter	N	Observation 1	Observation 2	p
EF	116	40 \pm 14%	40 \pm 14%	0.57
EDV	116	136 \pm 67 ml	136 \pm 65 ml	0.69
ESV	116	87 \pm 61 ml	87 \pm 60 ml	0.84

TABLE 3
Automated Motion-Mapped Compared with Manual Unmapped
Measurements: Linear Regression Results

Parameter	N	r	Intercept	Slope	SEE
EF	116	0.87	4.0%	0.96	7.2%
EDV	116	0.94	6.6 ml	0.93	22.6 ml
ESV	116	0.94	-0.4 ml	0.93	20.5 ml
ΔEF	116	0.21	-1.7%	0.11	7.0%
ΔEDV	116	0.03	-1.9 ml	-0.01	23.1 ml
ΔESV	116	0.03	-6.0 ml	-0.01	20.9 ml

dently on different occasions, with Pearson product-moment correlation coefficients, r, of 0.95 and with a slope of 0.98. Likewise, ED volume (EDV) and ES volume (ESV) reproducibility was very high (r = 0.98). Regression analysis of Bland-Altman plots revealed no significant trends, with absolute values of slopes of < 0.02 (Table 1). Mean EF values and EDVs and ESVs all agreed nearly perfectly (Table 2).

Manual Measurements

Comparing automatic motion-mapped measurements to manual values demonstrated good correlation both for EF (r = 0.87) and for ventricular volumes (r = 0.94) (Table 3). However, there was a weak trend (slope = 0.11) of the Bland-Altman plot for EF. This was confirmed by paired Student's t-test results between EF values showing that motion-mapped EF values were significantly (p = 8×10^{-5}) higher than manual EF values, by 3% (Table 4).

Accuracy

Automated motion-mapped EF values compared somewhat better (r = 0.90; slope = 0.87) to 22 correlative GFP EF values than did manual values (r = 0.85; slope = 0.68) (Table 5). Regression analysis of Bland-Altman plots revealed less of a trend for automated motion-mapped EF (r = 0.10; slope = -0.05) than for manual values (r = 0.40; slope = -0.24) (Table 5 and Fig. 6). The paired Student's t-test result again indicated a significant difference (p = 0.03) between motion-mapped EF (47% \pm 15%) and manual EF (44% \pm 12%). However, as the mean GFP EF (46% \pm 15%) fell midway between these two distributions, there was no statistically significant difference between GFP EF values and motion-mapped EF values (p = 0.33) or GFP EF values compared to manual EF values (p = 0.20). In comparing linear regression results, the Fisher Z-value was 0.76, with a high probability (p = 0.45) that motion-mapped and manual EF samples were derived from a population with the same degree of correlation to GFP measurements. Thus, on the basis of the Z-test, the apparent improvement in EF correlation to GFP values with motion-mapping was not statistically significant.

DISCUSSION

Automated motion-mapped ventricular function parameters were highly reproducible and correlated well with an expert's manual calculations and with independent first-pass measurements. The degree of agreement (r = 0.90; n = 22) of

TABLE 4
Automated Motion-Mapped Compared with Manual Unmapped
Measurements: Paired t-Test Results

Parameter	N	Motion-mapped	Manual	p
EF	116	40 \pm 14%	37 \pm 13%	8×10^{-5}
EDV	116	136 \pm 65 ml	140 \pm 66 ml	0.10
ESV	116	87 \pm 60 ml	94 \pm 60 ml	5×10^{-4}

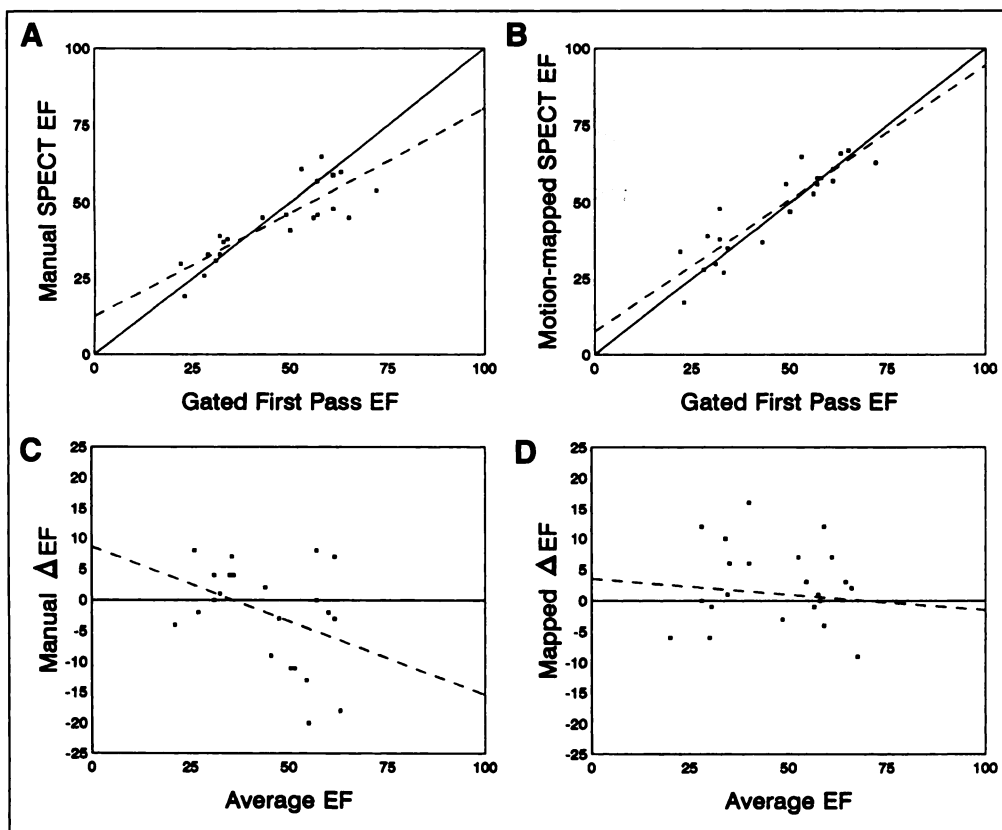


FIGURE 6. Linear regression plots of manual (A) and mapped (B) gated SPECT EF compared with GFP EF. Dashed lines are the least-squares fit, and the solid line is the line of identity. The differences, Δ EF, of (manual EF - GFP EF) compared with averages of these values are plotted in a Bland-Altman graph (C). The differences, Δ EF, of (mapped EF - GFP EF) versus EF averages are plotted in a Bland-Altman graph (D).

automated motion-mapped EF with GFP values is consistent with values found for comparisons between GFP data and gated SPECT methods based on Dodge-Sandler analogs ($r = 0.87$; $n = 38$) (11), relaxation labeling with wall thickening ($r = 0.73$; $n = 47$) (12) and Gaussian midmyocardial detection ($r = 0.91$; $n = 65$) (7). They are likewise similar to previous findings for automated gated SPECT Simpson's rule techniques ($r = 0.87$; $n = 65$) (9).

In addressing whether motion-mapped EF values were more accurate than manual values, comparison with GFP values demonstrated less of a trend of Bland-Altman plots ($r = 0.10$; slope = -0.05) than did manual values ($r = -0.24$; slope = -0.24), where $r = 0.0$ and slope = 0.0 would be ideal results (Fig. 6). Likewise, a higher degree of correlation ($r = 0.90$ compared with $r = 0.85$) with regression slopes nearer to unity (slope = 0.87 compared with slope = 0.68) and smaller error estimates (SEE = 4.5% versus SEE = 7.2%) were obtained for motion-mapped compared with GFP EF values than for manual values compared with GFP EF values, in which $r = 1.00$ and SEE = 0.0% constitute ideal results. However, all of these improvements were slight, as demonstrated by the Z-test result.

The clearest indication of the degree of difficulty in analyzing data such as that shown in Figure 1 is in the lower regression slope of 0.68 of the Bland-Altman graph (Fig. 6) for manual gated SPECT EF values compared with GFP EF values. The main advantage of performing the motion-mapping image transformation that was demonstrated numerically was in obtaining processing reproducibility for severely hypoperfused patient data (SEE = 4.5% ; $r = 0.95$; $n = 116$) (Table 1) comparable to previously reported results (SEE = 5.8% ; $r = 0.94$; $n = 126$) obtained for a wide spectrum of patients (9). These errors associated with repeated processing were also similar to those obtained for automated processing of gated SPECT data acquired on separate occasions in nonischemic patients (SEE = 5.5% ; $r = 0.92$; $n = 101$) (8).

In addition, eliminating the need to manually alter digital display contrast and brightness removes subjectivity of quality assurance both during processing and of final results. An advantage of motion-mapping is that it should provide the same degree of improvement in appreciation of myocardial shapes, regardless of which color scale is used, because of normalization of every ray at every angle in every cinematic frame. Independence from use of specific color tables should facilitate quality assurance because, previously, it was necessary to have simultaneous color and monochrome displays for optimal processing of severely hypoperfused data (3).

Limitations of this study include comparison of stress tomograms to resting first-pass studies. It has been shown that, in some ischemic patients, wall motion abnormalities can persist beyond 30 min poststress that are not necessarily present at rest (8,28). However, because only three of the first-pass patients studied here demonstrated significant exercise-induced ischemia, this is a minor concern. Algorithms presented here map the entire image, and consequently, 7 of the original 123 studies were discarded that demonstrated splanchic activity greatly in excess of adjacent severely hypoperfused inferior wall myocardial counts. Simple manual masking of input data to limit the search for radial input counts would have remedied this. A final drawback is that generating images of structures that strongly

TABLE 5
Gated SPECT Compared with Gated First-Pass EF:
Linear Regression Results

Method	N	r	Intercept (%)	Slope	SEE (%)
Mapped	22	0.90	7.5	0.87	6.5
Manual	22	0.85	12.5	0.68	6.7
Δ Mapped	22	0.10	3.5	-0.05	6.8
Δ Manual	22	0.40	8.6	-0.24	7.7

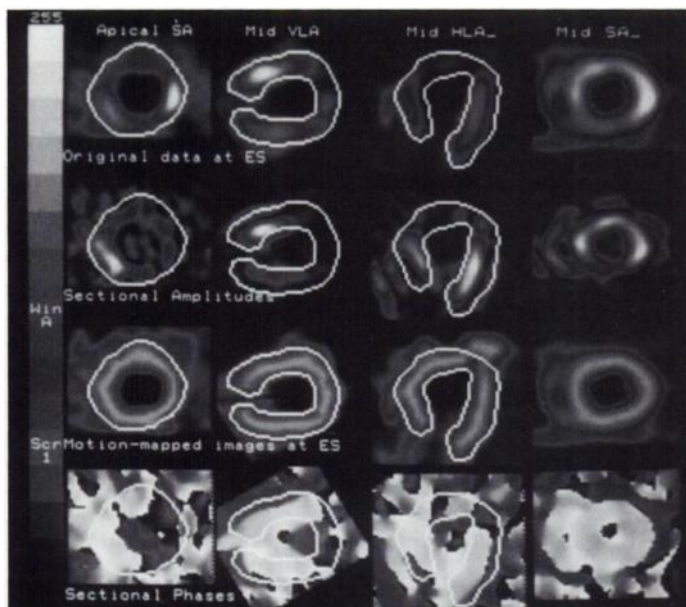


FIGURE 7. An example of motion-mapping contrast enhancement for the same patient shown in Figure 5. The top row shows original ES apical SA, midventricular VLA, midventricular HLA and midventricular SA axis images, from left to right. The second row shows the Fourier amplitude for each image set of the same column. The third row shows the motion-mapped transformed images, and the fourth (bottom) row shows corresponding Fourier phase images. Myocardial outlines drawn on the motion-mapped images are superimposed on all images.

suggest myocardial walls does not prove unequivocally that structures so revealed always are genuine myocardia and never artifacts. Further multimodality studies are warranted to verify directly that myocardial locations revealed by this motion-mapping algorithm agree with myocardia as seen on magnetic resonance images or echocardiograms.

The original motivation in investigating brightening-mapping was to make visible the intermediate steps inherent in gated SPECT techniques, which rely on myocardial perfusion count changes to locate endocardial surfaces (6,25,29). It was hoped that, by so doing, it would become clear why some studies found count-based gated SPECT EF methods to provide disappointing results for abnormal patients (25,29). Considerable care is needed in handling data of the lowest count density, containing the highest noise-to-signal ratio. Methods that implement Fourier time-filtering, intended to separate signal from noise in data representative of severe hypoperfusion (6), may not always prove helpful in depicting myocardia. This point is illustrated in Figure 7, showing an example of severely hypoperfused images and their motion-mapped transformations, along with associated Fourier amplitude and phase images. Clearly, only motion-mapped images provided shapes resembling myocardia. Thus, the motion-mapping algorithm greatly facilitates the ability of an observer to appreciate the location of myocardia, even when Fourier transformed images do not. Figure 7 also illustrates that even in cases of probable necrotic apical myocardia, accompanied by diverging apical walls, there are sufficient counts provided to the motion-mapping algorithm to generate a complete annular structure strongly suggestive of myocardium. It is not known at this time whether the small amounts of activity of such aneurysmal tissue are genuinely present or instead represent scatter of radiation from neighboring structures by unperfused tissue.

A potential concern of using this approach for edge detection is that it fails to take advantage of systolic count changes. These

can be significant in normal patients, accounting for different myocardial mass estimates derived from ED and ES tomograms (30). If partial volume effects linking count changes to myocardial thickening are linear (6,24,31), then the partial volume phenomenon should be useful in algorithms that relocate computed endocardial borders away from midmyocardial points within a cinematic frame (6,7). The approach pursued in this paper discards all impression of brightening and ignores the relationship between count density and wall thickness. However, the particular severely hypoperfused patient population studied here exhibited depressed EF values and large LV volumes, as would be expected (Table 4). Therefore, the degree of brightening was minimal for the data analyzed and would be expected to have the least influence on volumetric calculations from among potential patient groups. Furthermore, recent studies have shown that methods that only identify midmyocardial points without attempting to locate endocardial borders nonetheless produce gated SPECT EF values that agree well with gated blood pool equilibrium EF values (10) and that relaxation labeling models that use myocardial thickening to estimate endocardial borders produce results that are insensitive to errors in myocardial thickness assumptions (32). General questions of evaluating the degree to which motion-mapped images aid in visual appreciation of myocardial wall motion and of finding optimal means of combining myocardial brightening information with myocardial locations to estimate endocardial walls (29,33) remain, at the present time, active areas of research.

CONCLUSION

The motion-mapping image enhancement transformation produced consistent myocardial shapes throughout the heart cycle. This provided edge detection algorithms with highly predictable input and facilitated quality assurance of borders. As the technique is automatic, it simultaneously eliminated the need for an observer to manually adjust brightness and contrast displays to verify appropriateness of endocardial borders.

"Binary" image enhancement is used in some categories of algorithms, classifying every pixel into target (myocardial) and nontarget (nonmyocardial) areas (7,14). The algorithm presented here retains the contrast range of images and is applied to the entire radial extent of each image so that observers can appreciate all structures, including counts emanating from the right ventricle, spleen, liver, LV cavity and lung. Thus, this algorithm is intended not only to provide well-behaved input to edge detection software but also to simultaneously provide helpful images in perceiving wall translation. We anticipate that this algorithm will provide clinicians with a sensitive means of assessing regional wall motion abnormalities, both visually and quantitatively, in patients after myocardial infarction.

ACKNOWLEDGMENTS

This work was supported in part by a research grant from General Electric Medical Systems (Milwaukee, WI).

REFERENCES

1. Pryor DB, Harrel FE Jr, Lee KL, et al. Prognostic indicators from radionuclide angiography in medically treated patients with coronary artery disease. *Am J Cardiol* 1984;53:18-22.
2. Shah PK, Maddahi J, Staniloff HM, et al. Variable spectrum and prognostic implications of left and right ventricular ejection fractions in patients with and without clinical heart failure after acute myocardial infarction. *Am J Cardiol* 1986;58:387-393.
3. DePuey EG, Nichols K, Dobrinsky C. Left ventricular ejection fraction assessed from gated technetium-99m-sestamibi SPECT. *J Nucl Med* 1993;34:1871-1876.
4. Piriz JM, Kiernan FJ, Eldin A, et al. Correlation of left ventricular ejection fraction by gated SPECT ^{99m}Tc-sestamibi imaging with contrast ventriculography at subsequent cardiac catheterization [Abstract]. *J Nucl Med* 1996;37:105P.
5. Faber TL, Akers MS, Peshock RM, Corbett JR. Three-dimensional motion and perfusion quantification in gated SPECT. *J Nucl Med* 1991;32:2311-2317.

6. Cooke CD, Garcia EV, Cullom SJ, Faber TL, Pettigrew RI. Determining the accuracy of calculating systolic wall thickening using a fast Fourier transform approximation: a simulation study based on canine and patient data. *J Nucl Med* 1994;35:1185-1192.
7. Germano G, Kiat H, Kavanaugh PB, et al. Automatic quantification of ejection fraction from gated myocardial perfusion SPECT. *J Nucl Med* 1995;36:2138-2147.
8. Nichols K, DePuey EG, Salensky H, Rozanski A. Reproducibility of ejection fractions from stress versus rest gated perfusion SPECT [Abstract]. *J Nucl Med* 1996;37:115P.
9. Nichols K, DePuey EG, Rozanski A. Automation of gated tomographic left ventricular ejection fraction. *J Nucl Cardiol* 1996;3:475-482.
10. Everaert H, Franken PR, Flamen P, Momen A, Bossuyt A, Goris ML. Radial distribution of myocardial count rate density to measure left ventricular ejection fraction from gated perfusion SPECT studies [Abstract]. *J Nucl Med* 1996;37:211P.
11. Williams KA, Taillon LA. Left ventricular function in patients with coronary artery disease assessed by gated tomographic myocardial perfusion images: comparison with assessment by contrast ventriculography and first-pass radionuclide angiography. *J Am Coll Cardiol* 1996;27:173-181.
12. Vansant JP, Faber TL, Folks RD, Rao JM, Garcia EV. Resting left ventricular volumes and ejection fraction from gated SPECT: correlation to first pass [Abstract]. *Circulation* 1996;92(suppl 1):I-11.
13. Lefkowitz D, Nichols K, Rozanski A, Horowitz R, Mogtader A, DePuey EG. Echocardiographic validation of left ventricular volume measurements by ^{99m}Tc-sestamibi gated SPECT [Abstract]. *J Am Coll Cardiol* 1996;27:241A.
14. Faber TL, Stokely EM, Peshock RM, Corbett JR. A model-based four-dimensional left ventricular surface detector. *IEEE Trans Med Imaging* 1991;10:321-329.
15. Mullick R, Ezquerra NF. Automatic determination of LV orientation from SPECT data. *IEEE Trans Med Imaging* 1995;14:88-99.
16. Germano G, Kavanaugh PB, Chen J, et al. Operator-less processing of myocardial perfusion SPECT studies. *J Nucl Med* 1995;36:2127-2132.
17. DePuey EG. Artifacts in SPECT myocardial perfusion imaging. In: DePuey EG, Berman DS, Garcia EV, eds. *Cardiac SPECT*. New York: Raven Press; 1995:169-200.
18. DePuey EG, Rozanski A. Using gated technetium-99m-sestamibi SPECT to characterize fixed myocardial defects as infarct or artifact. *J Nucl Med* 1995;36:952-955.
19. Williams KA, Taillon LA. Reversible ischemia in severe stress technetium-99m-labeled sestamibi perfusion defects assessed from gated single-photon emission computed tomographic polar map Fourier analysis. *J Nucl Cardiol* 1995;2:199-206.
20. Van Train KF, Areeeda J, Garcia EV, et al. Quantitative same-day rest-stress technetium-99m-sestamibi SPECT: definition and validation of stress normal limits and criteria for abnormality. *J Nucl Med* 1993;34:1494-1502.
21. DePuey EG, Nichols KJ, Slowikowski JS, et al. Fast stress and rest acquisitions for technetium-99m-sestamibi separate-day SPECT. *J Nucl Med* 1995;36:569-574.
22. Nichols K, DePuey EG, Gooneratne N, Salensky H, Friedman M, Cochoff S. First-pass ventricular ejection fraction using a single crystal nuclear camera. *J Nucl Med* 1994;35:1292-1300.
23. Crawford CR. CT filtration aliasing artifacts. *IEEE Trans Med Imaging* 1991;10:99-102.
24. Hoffman EJ, Huang SC, Phelps ME. Quantitation in positron emission computed tomography. I. Effects of object size. *J Comput Assist Tomogr* 1979;5:391-400.
25. Gradel C, Staib LH, Heller EN, et al. Limitations of ECG-gated SPECT for assessment of regional thickening: experimental comparison with ECG-gated MRI [Abstract]. *J Am Coll Cardiol* 1996;27:241A.
26. Bland JM, Altman DG. Statistical methods for assessing agreement between two methods of clinical measurement. *Lancet* 1986;1:307-310.
27. Bland JM, Altman DG. A note on the use of the interclass correlation coefficient in the evaluation of agreement between two methods of measurement. *Comput Biol Med* 1990;20:337-340.
28. Johnson LL, Verdesca SA, Xavier RC, Chang KK, Nott LT, Noto RB. Postischemic stunning affects wall motion scores on poststress gated sestamibi tomograms [Abstract]. *J Am Coll Cardiol* 1996;27(suppl):241A.
29. Williams KA, Taillon LA. Five methods for evaluation of left ventricular function with ^{99m}Tc-sestamibi: a comparison with contrast ventriculography [Abstract]. *J Nucl Med* 1996;37:104P.
30. Williams KA, Lang RM, Reba RC, Taillon LA. Comparison of technetium-99m-sestamibi gated tomographic perfusion imaging with echocardiography and electrocardiography for determination of left ventricular mass. *Am J Cardiol* 1996;77:750-755.
31. Galt JR, Garcia EV, Robbins WL. Effects of myocardial wall thickness of SPECT quantification. *IEEE Trans Med Imaging* 1990;9:144-150.
32. Faber TL, Cooke CD, Vansant JP, Garcia EV. Sensitivity of an automated ejection fraction calculation from gated perfusion tomograms to modeling assumptions [Abstract]. *J Nucl Med* 1996;37:213P.
33. Buvat I, Bacharach SL, Bartlett ML, Yaroslavsky L. Wall thickening from gated SPECT/PET: evaluation of four methods [Abstract]. *J Nucl Med* 1995;36:8P.

Relationship of Decreased Chemotaxis of Technetium-99m-HMPAO-Labeled Lymphocytes to Apoptosis

C. Van de Wiele, J. Philippé, J.P. Van Haelst, J. Van Damme, H. Thierens, G.E. Leroux-Roels and R.A. Dierckx
 Division of Nuclear Medicine; Department of Clinical Chemistry, Clinical Microbiology and Immunology; and Department of Medical Physics, University Hospital Gent, Gent; REGA Institute, Laboratory of Molecular Immunology, University Leuven, Leuven, Belgium

The purpose of this study was to evaluate chemotaxis and its relationship to apoptosis in ^{99m}Tc-HMPAO-labeled lymphocytes. **Methods:** Peripheral lymphocytes, obtained from 12 healthy volunteers using lymphoprep, were divided in three equal fractions. One fraction was used as the control, one was labeled with cold HMPAO and one was labeled with 1.5 mCi (55.5 Mbc) ^{99m}Tc-HMPAO. Chemotaxis of T-lymphocytes was measured by the Boyden microchamber technique (BMA) (n = 8) using human monocyte chemoattractant protein-3 (MCP-3) as chemoattractants. A chemotactic index was calculated as the number of HMPAO and ^{99m}Tc-HMPAO-labeled cells that migrated towards the MCP-3 solution, divided by the number of nonlabeled migrated lymphocytes. Apoptosis evaluation (n = 10) of unlabeled, HMPAO-labeled and ^{99m}Tc-HMPAO-labeled cells was performed using flowcytometry (FCM) forward light scatter analysis, 900 light scatter analysis, fluorescein-isothiocyanate (FITC)-labeled Annexin V and dye exclusion of propidium iodide. **Results:** Chemotaxis of ^{99m}Tc-HMPAO-labeled T-lymphocytes was found to be reduced by approximately 31% (migration index of 0.69) (p = 0.01) as compared to both unlabeled and HMPAO-labeled lymphocytes, both the latter showing no difference in migration index. Whereas the mean percentages apoptotic lymphocytes in the unlabeled, 18.5%, and HMPAO-labeled fraction, 16.6%, were more or less comparable (p = 0.1), the mean percentage apoptotic cells in the ^{99m}Tc-HMPAO-labeled fraction was 51.8%, yielding a difference of 33.3% between ^{99m}Tc-HMPAO-labeled and unlabeled cells (p = 0.003). The percentual concordance between apoptotic cells (33.3%) and chemotactic impaired cells (31%) in the ^{99m}Tc-HMPAO-labeled fraction may be explained by the formation of a rigid cytoskeleton early in the apoptotic process that may theoretically limit chemotaxis. **Conclusion:** Using the BMA, chemotaxis of ^{99m}Tc-HMPAO-labeled lymphocytes was found to be reduced by approximately 31%. Furthermore, the percentage apoptotic lymphocytes induced by irradiation after labeling with ^{99m}Tc-HMPAO concurs well with the percentage of chemotaxis impaired cells.

Key Words: technetium-99m-HMPAO-labeled lymphocytes; apoptosis; chemotaxis

J Nucl Med 1997; 38:1417-1421

Controversy has surrounded the diagnostic value of labeling pure granulocytes as opposed to a mixed leukocyte population. In a study by Schauwecker et al. (1), comparing mixed leukocytes and pure granulocytes labeled in plasma, mixed leukocytes showed a slightly greater sensitivity for detecting

Received Sep. 23, 1996; revision accepted Jan. 28, 1997.
 For correspondence or reprints contact: C. Van de Wiele, Division of Nuclear Medicine, University Hospital of Gent, De Pintelaan 185, B-9000 Gent, Belgium.